Understanding Upper Water Mass Dynamics in the Gulf of Mexico by Linking Physical and Biogeochemical Features

Gabriela Yareli Cervantes-Díaz[a], José Martín Hernández-Ayón[b*], Alberto Zirino[c], Sharon Zinah Herzka[d], Víctor Camacho-Ibar[b], Orión Norzagaray[b], Leticia Barbero[e], Ivonne Montes[e], Joël Sudre[f], Juan Antonio Delgado[h]

[a] Facultad de Ciencias Marinas, Universidad Autónoma de Baja California, Transpeninsular Tijuana-Ensenada, No. 3917, Fraccionamiento Playitas, 22860. Ensenada, Baja California, México.

[b] Instituto de Investigaciones Oceanológicas, Universidad Autónoma de Baja California, Transpeninsular Tijuana-Ensenada, No. 3917, Fraccionamiento Playitas, 22860. Ensenada, Baja California, México.

[c] Scripps Institution of Oceanography, University of California, San Diego, 9500 Gilman Drive, La Jolla, California 92093, USA.

[d] Departamento de Oceanografía Biológica, Centro de Investigación Científica y de Educación Superior de Ensenada (CICESE), Baja California, Carretera Ensenada-Tijuana No. 3918, Zona Playitas, 22860, Ensenada, Baja California, México.

[e] NOAA Atlantic Oceanographic and Metereological Laboratory.

[f] Instituto Geofisico del Perú. Lima, Perú.

[g] LEGOS, CNRS/IRD/UPS/CNES UMR 5566, 18 av. Ed Belin, 31401 Toulouse Cedex 9, France.

[h]Tecnológico Nacional de México/campus Guaymas, Km 4 S/N, Carretera al Varadero Nacional, Sector Playitas, 85480, Guaymas, Sonora, México.

*__Corresponding author:__ J.M. Hernández-Ayón (jmartin@uabc.edu.mx)

ORCID ID: 0000-0001-6869--

Abbreviations: absolute salinity (S_A), absolute dynamic topography (ADT), apparent oxygen utilization (AOU), Antarctic Intermediate Water (AAIW), Caribbean Surface Water (CSW), Caribbean Water (CW), Caribbean Surface Water remnant (CSWr), Campeche Bay (CB), conservative temperature (Θ), coefficient of variation (CV), dissolved inorganic carbon (DIC), dissolved oxygen (DO), density anomaly (σ_θ), Gulf Common Water (GCW), Gulf of Mexico (GoM), Loop Current (LC), Loop Current eddies (LCEs), North Atlantic Subtropical Underwater (NASUW, herein referred to as SUW), North Atlantic Deep Water (NADW), Potential temperature (T_θ), salinity (S), Tropical Atlantic Central Water (TACW).

Abstract

In the Gulf of Mexico (GoM), the upper 300 m of the water column contains a mixture of water types derived from water masses from the North Atlantic and the Caribbean Sea, namely Caribbean Surface Water (CSW), Subtropical Underwater (SUW), Gulf Common Water (GCW), and Tropical Atlantic Central Water (TACW). These are mainly altered by mesoscale processes and local evaporation, which modulate biogeochemical cycles. In this study, we improve our understanding of water mass dynamics by including biogeochemical data when evaluating the T-S relationship to define water-mass boundaries, particularly when the observed thermohaline characteristics overlap. The variables considered were apparent oxygen utilization (AOU), nitrate, and dissolved inorganic carbon (DIC). The data were obtained from eight cruises carried out in the central and southern regions of the GoM and an additional cruise that covered the entire coastal-ocean region. The new proposed boundaries were instrumental in clarifying the dynamics of surface waters. Of note, GCW on the western side of the GoM is not formed from the mixing of CSW and SUW but by the mixing of remnant CSW with TACW. In winter, a remnant of CSW mixed with GCW, and the biogeochemical composition of surface waters was affected, as observed from an increase in nitrate and DIC concentrations and positive AOU values. CSW was mainly detected at the surface during summer with negative AOU values, low DIC values, and almost undetectable nitrate concentrations. The presence or absence of CSW modulated the depth of the nitracline and likely influenced primary productivity.

Keywords: Water mass, apparent oxygen utilization, biogeochemistry, isopycnal, anticyclonic eddy, Gulf of Mexico

1 Introduction

Forecasting the effects of global warming on ocean resources depends on a clear understanding of how physical processes, such as the radiation balance, advection, and mixing, interact with local biogeochemical activity.

1.1 Summary of Water Mass Interactions in the Gulf of Mexico (GoM)

The Gulf of Mexico (GoM) contains a mixture of water types derived from the North Atlantic and Caribbean Sea (Schmitz and Richardson, 1991), and its deep waters contain North Atlantic Deep Water (NADW) overlain by Antarctic Intermediate Water (AAIW) and Tropical Atlantic Central Water (TACW; Portela et al., 2018). However, upper surface water in the GoM can be considered a mixture of three main water types that may be identified by temperature (T)-salinity (S) relationships, namely Caribbean Surface Water (CSW), Gulf Common Water (GCW), and North Atlantic Subtropical Underwater (NASUW, hereafter referred to as SUW), which are all found above a sigma-theta level of ~ 26 $kg \cdot m^{-3}$ (Fig. 1; Portela et al., 2018). These water types are altered by local evaporation and dilution due to riverine freshwater inputs that mainly stem from the Mississippi-Atchafalaya system and Mexican rivers in the southern region of the GoM. Likewise, GCW is considered to be a mix of only CSW and SUW, as its salinity does not change significantly (Vidal et al., 1992). However, at higher sigma-theta values (relative values of 26.5 $kg \cdot m^{-3}$), all three types converge into the TACW water mass with a linear T-S relationship (Fig. 1).

Surface circulation in the central GoM is complex and dominated by the dynamics of the Loop Current (LC) and its associated eddies (Sturges and Leben, 2000; Oey et al., 2005), which transport CSW into the gulf as a remnant of Caribbean Surface Water (CSWr), as classified by Portela et al. (2018). Unmodified CSW can be found in the Yucatan Strait, LC, and eddies (see Fig. 1a, black T-S line). Upon entering the GoM, CSW is characterized by high S values of ~ 34.5 to 36.6, potential temperature (T_θ) $\geq$ 25 ºC, and potential density (σ_θ) $\leq$ 24.5 $kg \cdot m^{-3}$, as reported by Carrillo et al. (2016). Anticyclonic Loop Current eddies (LCEs) that are ~ 200–300 km in diameter detach from the LC every 4–18 months (Sturges and Leben, 2000; Hall and Leben, 2016) and may reattach (Schmitz, 2005). Other key features of GoM dynamics are the intrusion and variable position of the LC (Bunge et al., 2002; Delgado et al., 2019). The annual intrusion of the LC is statistically more likely during spring and summer when it can extend to ~ 28º N and 90.5º W, whereas during autumn and winter, there is little LC incursion into the GoM (Delgado et al., 2019).

Near the surface, the chemical and biological properties of CSW are reflected in the spatial variability of T, S, dissolved oxygen (DO), freshwater inputs, the heat flux, evaporation, and wind stress, which are also related to the presence of the LC and LCEs (see Fig. 1a, b; Morey et al., 2003b; Portela et al., 2018; Damien et al., 2018). A major contributing factor to surface thermohaline variability in the northern GoM is the Mississippi-Atchafalaya river system, which influences the upper 50 m of the water column in areas hundreds of kilometers away from its discharge zone (Morey et al., 2003a; Jochens and DiMarco, 2008; Portela et al., 2018). These mechanisms, as mentioned earlier, influence the chemical, biological, and physical water mass characteristics above the 26 $kg \cdot m^{-3}$ isopycnal.

In the region influenced by the LC, SUW can be identified by S values between 36.5 to 36.92 at ~ 100–150 m, which is below the depth of CSW (Herring, 2010; Hamilton et al., 2018). Properties representative of incoming SUW with maximum S values of > 36.92 can be observed in the Yucatan Strait (Fig. 1a, c, black and red dots). However, once inside the GoM, SUW likely loses its thermohaline properties because the GoM is an evaporative basin in which convective mixing modifies the characteristics of existing surface waters, and Gulf Common Water (GCW) is supposedly formed within (Vidal et al., 1992). In addition, LC surface water is considered oligotrophic given its relative isolation from the eutrophic waters of the coast and continental shelf (Biggs and Ressler, 2001; Heileman and Rabalais, 2009; Damien et al., 2018; Martínez-López and Zavala-Hidalgo, 2009). Within the LC (0–90 m depth), the concentrations of nitrate, phosphate, and other essential nutrients are usually below the analytical detection limit (< 0.05 μM; Biggs and Ressler, 2001). Far from the coast, primary production < 0.15 g C m^{-2} d^{-1} has been reported (Biggs and Ressler 2001), while productivity in subsurface waters might be 2- to 3-fold higher when nutrient availability is locally enhanced (El-Sayed, 1972; Biggs and Ressler, 2001).

Previous studies (i.e., Portela et al., 2018; Hamilton et al., 2018) have presented different thermohaline limits for GoM water masses given their primary focus on deep waters (σ_θ > 26 $kg \cdot m^{-3}$; Fig. 1a). However, a more detailed classification system for the waters above the 26 $kg \cdot m^{-3}$ isopycnal is necessary, as these waters are significantly modified by various factors like mesoscale structures, river inputs, wind-driven mixing, evaporation, and precipitation. If biogeochemical properties are considered in addition to thermohaline properties when water masses are defined, water mass dynamics would be better understood. A point of concern regarding the water mass dynamics of the GoM is related to the formation of GCW. When only thermohaline properties are considered, it has been proposed that the formation of GCW is mainly due to the mixing of LCE waters and the dilution of SUW (Vidal et al., 1994; Portela et al., 2018).

GCW is distinguished by a relatively homogeneous vertical S distribution, ranging from 36.3–36.49 from ~ 0–200 m depth (Merrell and Morrison, 1981; Elliott, 1982; Morrison et al., 1983). The apparent oxygen utilization (AOU) shown in Figure 1b indicates a gradual trend towards negative concentrations above the 26 $kg \cdot m^{-3}$ isopycnal. In addition, the AOU concentrations of GCW and SUW are similar and in the range of 40–70 $\mu mol \cdot kg^{-1}$, and they differ from those of TACW, which is located below and characterized by DO concentrations of ~ 3 $ml \cdot L^{-1}$, Tθ values from 7.9–20 °C, and S values between 34.9–36.4 around the 27.2 $kg \cdot m^{-3}$ isopycnal (Vidal et al., 1994; Gallegos, 1996; Carrillo et al., 2016; Portela et al., 2018). However, TACW may share properties with both surface water bodies as a result of mixing processes. All of these issues point toward the challenges related to adequately understanding and determining the formation of GCW and evaluating the spatial distributions of GCW and SUW.

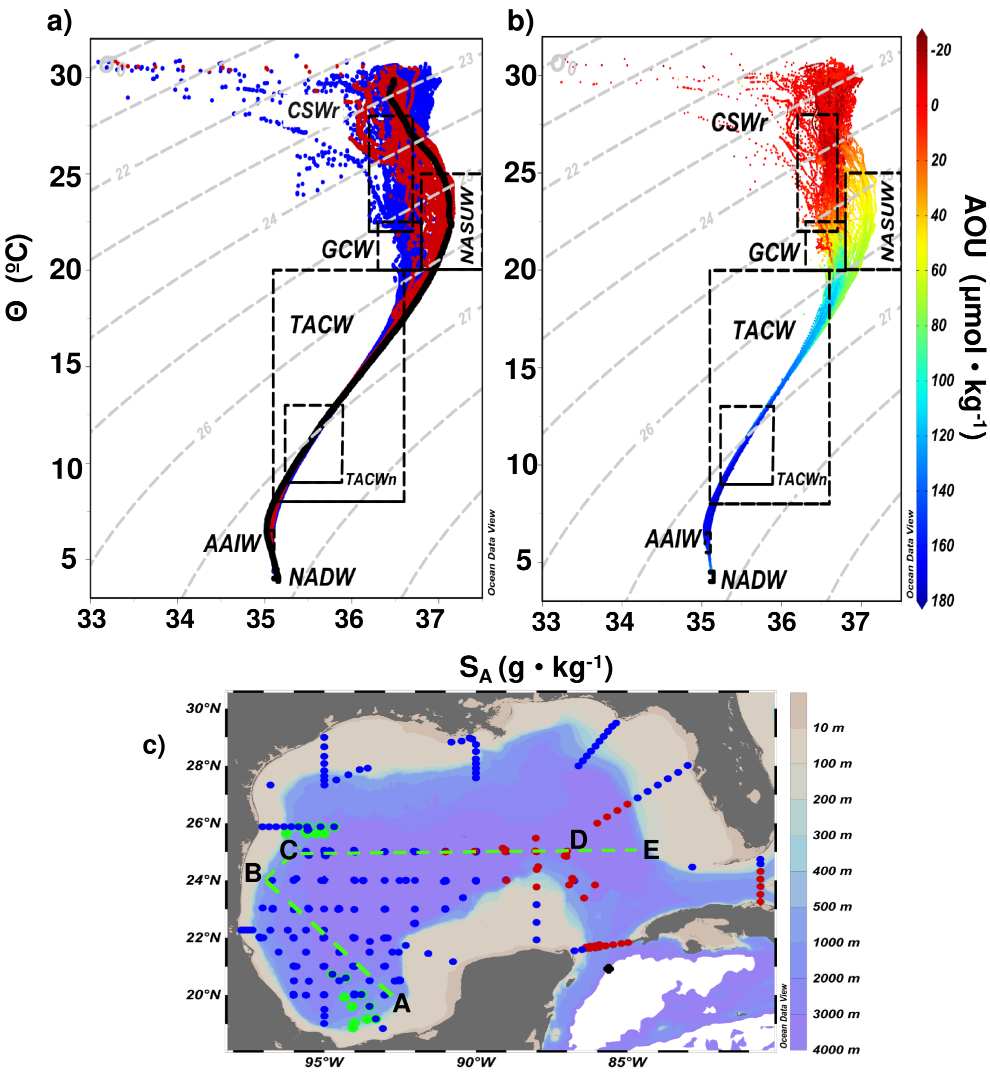

Fig. 1 Conservative temperature (Θ)-absolute salinity (S_A) diagrams of data from the six XIXIMI (2010–2017) and GOMECC-3 (2017) cruises. (a) Distribution of the water masses based on the classification proposed by Portela et al. (2018) using Θ and S_A ($g \cdot kg^{-1}$). Water masses: Caribbean Surface Water remnant (CSWr), North Atlantic Subtropical Underwater (NASUW), Gulf Common Water (GCW), Tropical Atlantic Central Water (TACW), TACWn (core), Antarctic Intermediate Water (AAIW), and North Atlantic Deep Water (NADW). (b) Θ-S_A diagram and apparent oxygen utilization (AOU, $\mu mol \cdot kg^{-1}$) diagram. (c) The stations included are depicted with red and blue dots. The red dots denote the stations where the signal characteristic of NASUW was detected. The black dot outside the GoM denotes the endmember with the unmodified characteristics of Caribbean Water, while the blue dots indicate stations with characteristics of LC incursion. Stations delimited by green lines and black letters constitute fixed transects throughout this paper. The stations covered during the two other Perdido (letter C) and Coatzacoalcos (letter A) cruises are represented by green dots.

This study improves our understanding of how GCW is formed and the spatial distribution of SUW inside the GoM. We suggest a reclassification of surface water mass limits above the 26 $kg \cdot m^{-3}$ isopycnal, particularly when the observed thermohaline characteristics overlap, by including biochemical data to obtain a more precise definition of the boundaries of CSW, SUW, and GCW. In addition, we aimed to identify the biogeochemical implications of thermohaline changes in surface waters due to an increasing extension of the LC, which carries water of Caribbean origin into the GoM, and the potential effects on the depth of the nitracline. Finally, we confirm the role that CSW plays in the biogeochemistry of the GoM by comparing measured seasonal variations in T_θ, S, nitrate, and AOU to those of the CARS2009 climatological database (CSIRO Atlas of Regional Seas; http://www.marine.csiro.au/~dunn/cars2009).

2 Materials and Methods

2.1 Data collection

Six oceanographic cruises covering the central and southern regions of the Exclusive Economic Zone of Mexico were carried out in November 2010, July 2011, February–March 2013, August–September 2015, July 2016, and August–September 2017 (XIXIMI-01–XIXIMI-06, respectively) onboard the R/V *Justo Sierra* (Fig. 1c). In addition, two oceanographic cruises (March and September 2016) that covered the Perdido region (~ 26° N) in the northwestern gulf and the Coatzacoalcos regions in Campeche Bay (CB, ~ 94° W) were added (Fig. 1c). During these campaigns, 30–51 stations per cruise were sampled, and a total of 519 hydrographic casts were performed to characterize the vertical distribution of T_θ, S, σ_θ, DO, and fluorescence. An SBE 911plus CTD (Sea-Bird Electronics, Inc., Bellevue, USA) was used. The instrument and sensors were regularly serviced and calibrated before the XIXIMI cruises. For the two cruises in Perdido and Coatzacoalcos, an SBE 25plus CTD with a nitrate SUNA Atlantic sensor (Sea-Bird Electronics, Inc.) was used at 19 stations. Finally, data from the third Gulf of Mexico Ecosystems and Carbon Cycle (GOMECC-3) Cruise were included. The GOMECC-3 cruise was funded by the National Oceanic and Atmospheric Administration (NOAA) Ocean Acidification Program and took place on board the NOAA Vessel *Ronald H. Brown* (July 18–August 21, 2017). GOMECC-3 covered stations that ran along nine transects within the entire gulf as well as the Yucatan Channel and Florida Straits (Fig. 1c). The GOMECC-3 CTD package consisted of a Sea-Bird Electronics (SBE) 9 plus CTD with dual pumps and the following sensors: dual temperature (SBE3), dual conductivity (SBE4), dual dissolved oxygen (SBE43), reference temperature (SBE35), a Wet Labs CSTAR transmissometer, and a Valeport VA500 altimeter (Barbero et al., 2019).

In addition to CTD casts, water samples were collected with 10- or 20-L Niskin bottles at 12–24 set depths, depending on the cruise, to measure DIC, nutrient, and DO concentrations, among other parameters. Dickson et al. (2007) established protocols that were followed in addition to best practices for DIC sample collection and analysis. To collect nutrient samples, 50 mL of seawater was filtered through Whatman GF/F filters (GE Healthcare, Chicago, USA) that had been previously combusted at 450 °C for 2 h. The filtered samples were transferred to centrifuge tubes, frozen, and transported to the laboratory for post-cruise analysis. In the GOMECC-3 cruise, nutrient samples were analyzed onboard, following procedures detailed in the updated GO-SHIP Repeat Hydrography Manual (Becker et al., 2019). During each cruise, seawater was also routinely sampled to determine DO concentrations with the Winkler method as a quality control of the CTD oxygen probe (Baird and Bridgewater, 2017).

Additionally, AOU (µmol·kg^{-1}) was calculated from DO, T_θ, and S using the TEOS-2010 equations (Intergovernmental Oceanographic Commission, 2010). However, it must be recognized that the calculation of AOU is affected by processes other than those that are biochemical, such as water mixing, deviations of DO concentrations from instantaneous and complete equilibrium with the atmosphere and other factors (Pytkowicx 1971; Broecker and Peng, 1982; Garcia and Keeling, 2001; Ito, 2004). Thus, AOU calculation involves T and S compensation, producing a value corrected for thermodynamic effects on DO.

2.2 *Water mass characterization*

An analysis of T_θ-S diagrams was carried out for the six XIXIMI cruises (Fig. 1c), for which T_θ and S were converted to conservative temperature (Θ) and absolute salinity (S_A), as described by McDougall and Barker (2011).

Given that two XIXIMI cruises took place during late fall and winter (2010 and 2013) while the remaining four took place during summer (2011, 2015, 2016, and 2017), we performed separate seasonal analyses of the hydrographic and biogeochemical characteristics of seawater above isopycnals < 26 kg·m^{-3} in the Θ-S_A diagrams using the Portela et al. (2018) classification (Fig. 2). In addition, AOU was incorporated into the diagrams to evaluate the role of seasonality on its vertical distribution given the water masses present. The most notable variability in the water column was present above the 26 kg·m^{-3} isopycnal. The depth of this isopycnal varied by more than 100 m during the summer due to the presence of LCEs, while variation was lower during the winter when fewer sampling stations were located within anticyclonic eddies (Fig. A.1).

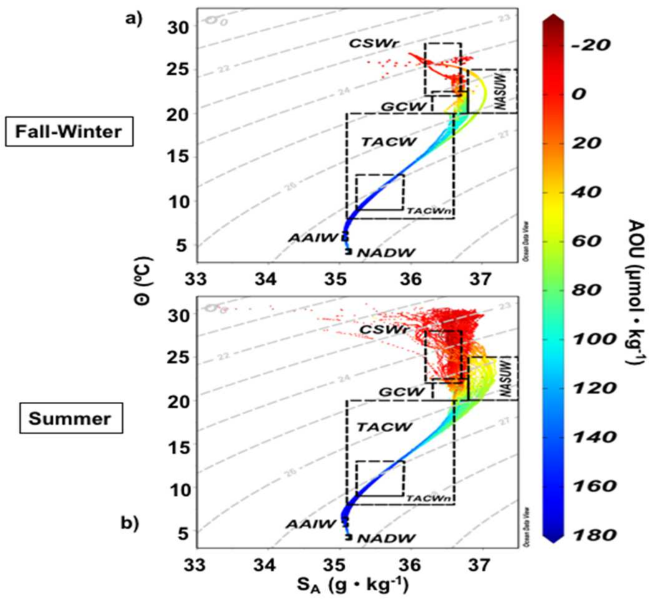

Fig. 2 Θ-SA vs. apparent oxygen utilization (AOU; µmol·kg^{-1}) diagrams in late fall–winter (a) and summer (b), along with the water mass classification by Portela et al. (2018): CSWr,

NASUW, GCW, TACW, TACWn (core), AAIW, and NADW. To generate the Θ-S_A vs. AOU ($\mu mol \cdot kg^{-1}$) diagrams, we used data from the six XIXIMI cruises. The late fall and winter cruises (2010 – 2013) were separate from the summer cruises (2011, 2105, 2016, and 2017).

A separate analysis of the Θ-S_A diagrams was carried out with the data collected during the Perdido and Coatzacoalcos cruises of spring–summer 2016. CTD-derived NO_3^- concentrations and AOU estimates were incorporated into each decibar of resolution. Also, the samples collected at standard depths corresponding to the XIXIMI and GOMECC-3 cruises (late fall 2010, winter 2013, and summer 2016 and 2017) were incorporated into the analysis of the Θ-S_A diagrams. Finally, the Θ-S_A diagrams were compared to the Portela et al. (2018) classification.

Density vs. nitrate concentration graphs were plotted with AOU on a third axis to evaluate the relationships between density fields and 1) oligotrophic waters (values < 1.0 $\mu mol \cdot kg^{-1}$); 2) the nitracline (values >1.0 $\mu mol \cdot kg^{-1}$); and 3) AOU (negative values ± 20 $\mu mol \cdot kg^{-1}$). We then readjusted the thermohaline ranges of the water masses based on the combined characteristics of the thermohaline and biogeochemical (nitrate and AOU) variables at $\sigma_\theta < 26$ $kg \cdot m^{-3}$ for each identified water mass. Finally, vertical distribution sections for σ_θ, T_θ, and AOU were constructed for all nine cruises (Perdido and Coatzacoalcos, XIXIMI-1–6, and GOMECC-3) to evaluate differences arising from different seasonal oceanographic conditions.

2.3 Analysis of chemical variables

Coulometric methods were used following the methodology of Johnson et al. (1987) for determining DIC concentrations. Reference materials were provided by the laboratory of Dr. A. Dickson of the Scripps Institution of Oceanography. The accuracy obtained for the reference material was ± 2 $\mu mol \cdot kg^{-1}$ with a precision of ± 1.5 $\mu mol \cdot kg^{-1}$. In addition, DIC and nitrate (NO_2^- + NO_3^-) analyses corresponding to the GOMECC-3 cruise were carried out following the GO-SHIP Hydro Manual (https://www.go-ship.org/HydroMan.html) and are described in detail in Barbero et al. (2019).

To quantify the concentrations of combined nitrite and nitrate (NO_2^- + NO_3^-, hereafter nitrate) present in the samples from the 2010 and 2013 winter cruises, a Skalar SAN Plus autoanalyzer (Skalar Analytical, Breda, Netherlands) was used. In addition, the reference material for nutrients, MOOS-2 (certified concentration of 24.9 ± 1 μM) obtained from the National Resource Council of Canada, was repeatedly analyzed during runs to evaluate accuracy and precision. As a result, the average recovery for the analyses of the three cruises was 25.1 ± 0.25 $\mu mol \cdot kg^{-1}$. For summer 2015, the samples were analyzed with an AA3-HR SEAL nutrient analyzer (SEAL Analytical Inc., Mequon, USA) according to the GO-SHIP Repeat Hydrography Manual (Hydes et al., 2010) using seawater lots CC (with a calculated certified value for NO_2^- + NO_3^- of 30.99 ± 0.24 $\mu mol \cdot kg^{-1}$) and CD (with a calculated certified value for NO_2^- + NO_3^- of 5.52 ± 0.05 $\mu mol \cdot kg^{-1}$) from Kanso Co. Ltd. (Kanso Technos, Tokyo, Japan) as reference materials (see description in Aoyama and Hydes, 2010). The average recoveries for NO_2^- + NO_3^- - during the analyses of the three cruises were 30.88 ± 0.10 and 5.50 ± 0.03 $\mu mol \cdot kg^{-1}$ for RMNS CC and CD, respectively.

In addition, the CTD 25plus included a UV sensor for nitrate determination (SUNA, Satlantic, Halifax, Canada; ± 2.4 μM). To determine the nitrate concentrations, a factory calibration was used. Nitrate data were coupled to CTD profiles using cast time. Since the SUNA data showed high variability (spectral analysis indicated that the most frequent variability periods were observed between 2–6 m in the vertical profiles), a low-pass filter was applied using a 15-m data window. The filter and data window were selected based on the lowest noise to signal ratio and coefficient of variation observed. Filtered nitrate profiles obtained with the SUNA sensor were contrasted with discrete sample profiles using simple linear regressions, obtaining significant models and coefficients ($p < 0.05$; $n = 33$; average $r^2 = 0.97 \pm 0.05$; average slope = 0.94 ± 0.15), which indicated good correspondence between both measurements. This analysis was exclusively conducted for the Perdido and Coatzacoalcos cruises.

To explore possible relationships between the water masses and their nitrate and DIC concentrations, three-phase T_θ-S diagrams (in which the colors indicate nitrate concentrations) were constructed for the late fall-winter-spring period of 2010, 2013, and 2016 and the summers of 2015, 2016, and 2017. Also, T_θ-S vs. DIC diagrams for late fall–winter and summer 2011, 2015, 2016, and 2017 were constructed for a seasonal comparison.

2.4 Absolute dynamic topography (ADT) maps

Absolute dynamic topography (ADT; cm) maps were generated to evaluate the influence of CSW on water mass characteristics during the different cruises, as described by Delgado et al. (2019). The images were products of the AVISO+ database (https://www.aviso.altimetry.fr/en/data). The ADT maps only considered the period in which sampling was carried out for each cruise. For simplicity, we present ADT maps for two cruises held during contrasting conditions (Fig. 9b and e): winter (Feb–Mar 2013) and summer (Aug–Sep 2015).

2.5 Climatological data analysis

A comparative analysis of the average T and S data from the CARS 2009 (CSIRO Atlas of Regional Seas; http://www.marine.csiro.au/~dunn/cars2009) database was conducted to determine if the climatological data were consistent with the observations made during winter (February) and summer (July). The rationale for this analysis was that CSW was mainly detected during summer at the surface, whereas GCW replaced CSW in winter, which was reflected in the biogeochemical composition near the surface. Diagrams and vertical sections based on 50 years of T_θ and S data for July and February were plotted to confirm the presence of the LC front (Fig. A.3).

3 Results

3.1 New thermohaline and isopycnal limits of near-surface water masses

Our study revealed several important features using the water mass classification of Portela et al. (2018). Firstly, all data above 28°C and below 23.5 $kg \cdot m^{-3}$ were excluded from the classification. Secondly, an overlap region between the limits of CSWr and GCW was present. It should be noted that within these overlaps, large differences in nitrate and DIC concentrations were observed, ranging from 5–0.5 $\mu mol \cdot kg^{-1}$ and from 2155–2020 $\mu mol \cdot kg^{-1}$, respectively (Fig. 3). Thirdly, at σ_θ lower than ~ 25 $kg \cdot m^{-3}$, AOU values were slightly positive or closer to zero than those above 25 $kg \cdot m^{-3}$ (Fig. 1b). Similarly, the lowest DIC concentrations and nearly depleted nitrate concentrations were observed at densities lower than 25 $kg \cdot m^{-3}$ (Fig. 3). Finally, CSW had lower nitrate, AOU, and DIC concentrations than those of SUW and GCW (Fig. 1 and 3; Table 1).

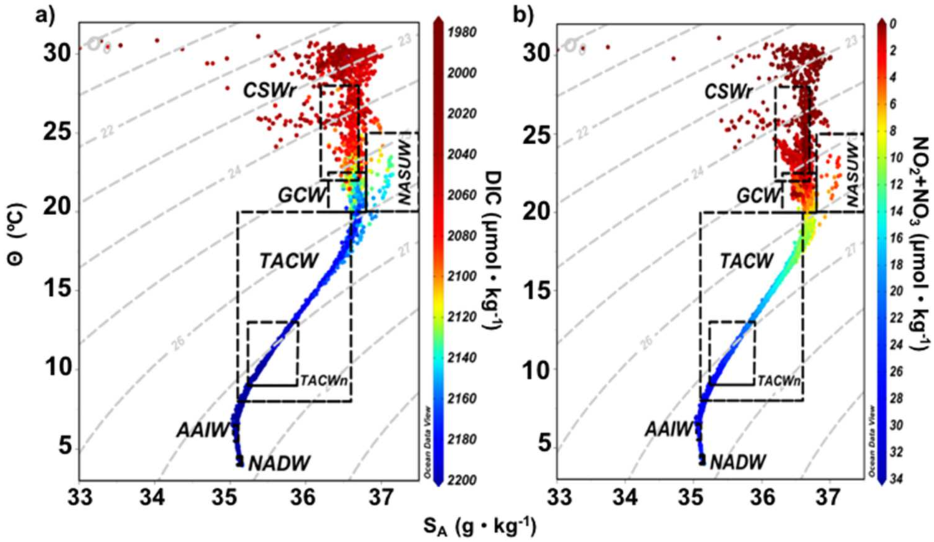

Fig. 3 Analyses of the Θ-S_A diagrams were conducted for spring–summer 2016 of the Perdido, Coatzacoalcos, XIXIMI cruises (late fall 2010, winter 2013, and summer 2016 and 2017), and GOMMEC-3 cruise (summer 2017). This analysis included NO_3^- (SUNA sensor and discrete samples) and inorganic dissolved carbon (DIC) concentrations. (a) Θ-S_A and DIC (μmol·kg^{-1}) and (b) Θ-S_A and NO_2^-+NO_3^- (μmol·kg^{-1}) diagrams as well as the Portela et al. (2018) water mass classification.

At σ_θ below 26 kg·m^{-3}, a clear biogeochemical signal is observed for the three upper water masses of the GoM (Fig. 4). We were able to detect when changes occurred with great precision given that continuous CTD sensor data, including nitrate and oxygen information for two cruises, was utilized. For example, Fig. 4a indicates a difference in nitrate at 25.3 kg·m^{-3} while also showing that nitrate concentrations do not exceed 1 umol·kg^{-1} at sigma theta values > 25 kg·m^{-3} and < 25.5 kg·m^{-3}. Therefore, σ_θ below 25.3 kg·m^{-3} is a useful boundary between CSW, GCW, and SUW. A nitrate concentration < 1 μmol·kg^{-1} (with a detection limit range of ± 1 μmol·kg^{-1}) and slightly negative or near to zero AOU values (with a detection limit range of ± 20 μmol·kg^{-1}), acted as tracers for this water mass, indicating the boundaries at which CSW began (Fig. 4a-d). In addition, CSW was found to possess low DIC concentrations, with values less than 2140 μmol·kg^{-1} (Fig. 3a, Table 1).

These clear patterns also helped simplify the determination of the upper limit of GCW and indicated that the isopycnals between 25.3–26.3 kg·m^{-3}, where the nitracline is found, and positive AOU values were considered characteristic of GCW (Fig. 4a–b; Table 1). A typical increase in nitrate (> 1 μmol·kg^{-1}) with increasing depth was observed. This pattern was also observed for AOU concentrations (> 20 μmol·kg^{-1}). GCW was also characterized by higher DIC concentrations (~ 30 μmol·kg^{-1} higher) than those of CSW (Table 1). In particular, CSW presented the lowest DIC concentrations of all, with values < 2140 μmol·kg^{-1} (Fig. 3a; Table 1).

The limit of SUW is located between the isopycnals of 24.5–26.5 kg·m^{-3} (Fig. 3 and 4), and the distribution of SUW within the GoM was noted to be linked to LC incursion (Fig. 1a and c). However, the salinity maximum of SUW lies in a separate part of the T-S plot, as it is derived from a well-defined layer (Fig. 1). The biogeochemical signals of SUW also fall in a separate section of the T-S plot, where nitrate values ranged between 1–8 µmol·kg^{-1} with increasing depth, and AOU values were considered to be characteristic between 0–120 µmol·kg^{-1}. Thus, SUW presented higher DIC concentrations than those of CSW but lower than those of GCW, with values of ~ 2100 µmol·kg^{-1} (Fig. 4b–c; Table 1).

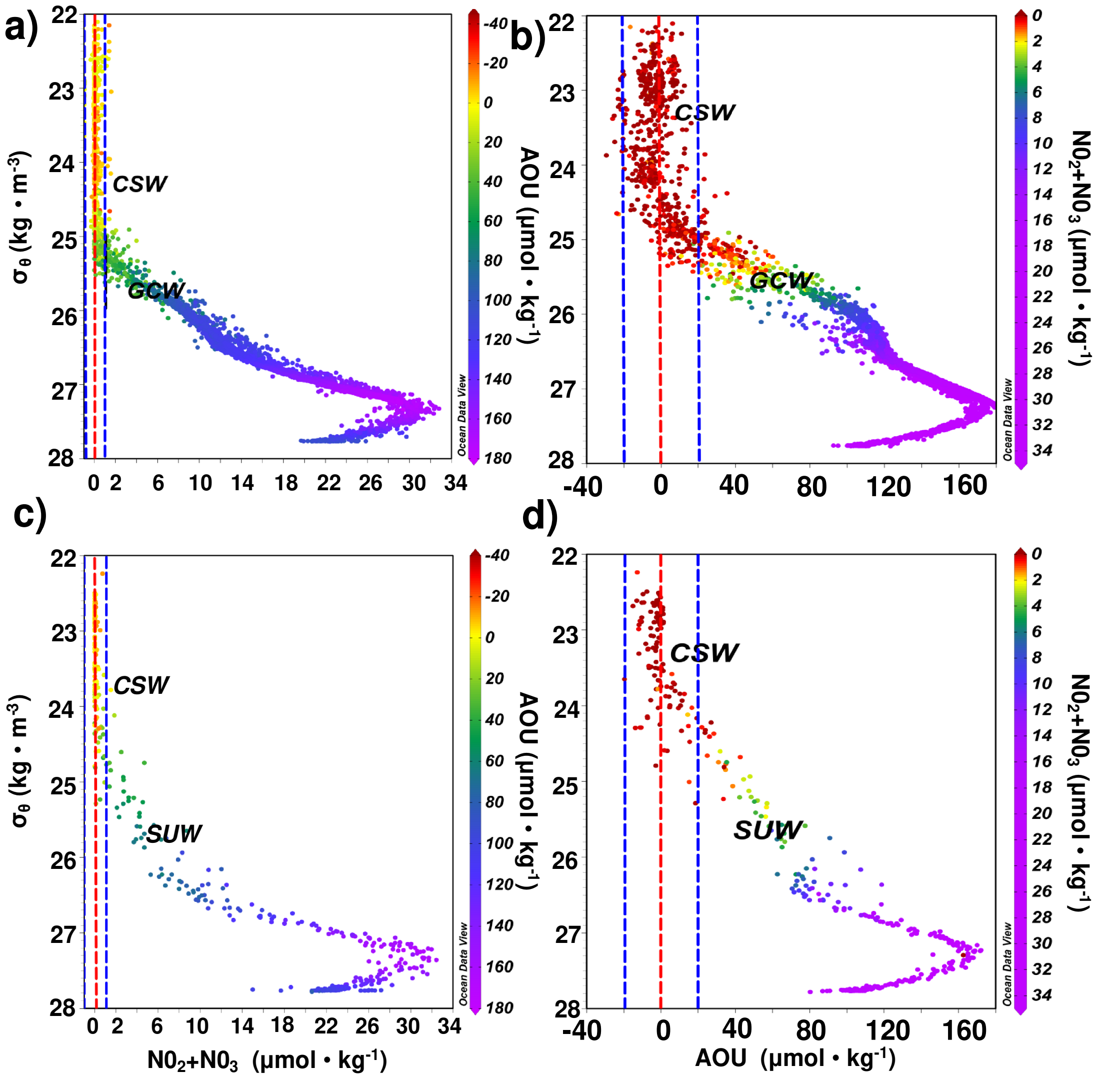

Fig. 4 Relationships among potential density (σ_θ), apparent oxygen utilization (AOU), and nitrate concentrations for the Perdido, Coatzacoalcos (both CTD and nitrate SUNA data), XIXIMI, and GOMECC-3 cruises (discrete samples at standard depths). Figures a and b represent the data located in the western part of the GoM and are shown in blue in Figures 1a, c. Figures b and c represent the data located in the portion of the GoM under the influence of the LC and are shown in red in Figure 1a, c. The red vertical line shows both the zero-nitrate and zero-AOU

concentration limits, and the blue lines denote the detection limits of the nitrate and oxygen sensors.

We propose adding biogeochemical data to the T-S relationship to better define the boundaries of the water types, particularly when the observed thermohaline characteristics overlap. Based on this, new thermohaline and σ_θ ranges are proposed based on the σ_θ, nitrate, AOU, and DIC criteria (Fig. 5; Table 1). Firstly, low σ_θ, warm, and oligotrophic waters with negative AOU values defined the limit of CSW (Figs. 4 and 5). In contrast, subsurface waters associated with GCW showed an apparent increase in nitrate, accompanied by positive AOU values closely related to TACW mixing.

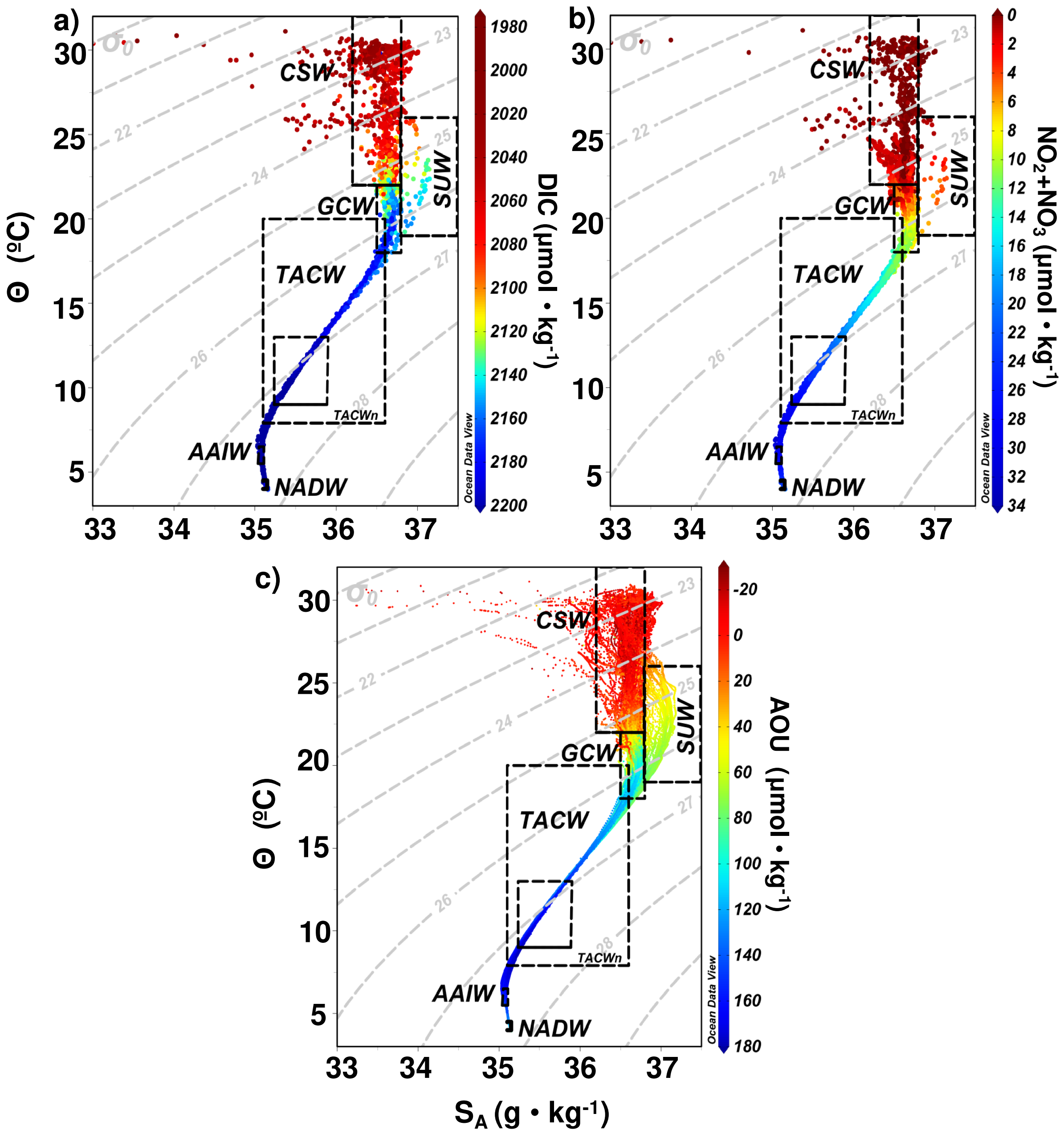

Fig. 5 Reclassification of the thermohaline limits for water masses based on the distribution of biogeochemical characteristics [AOU and $NO_2^- + NO_3^-$] shown in Figure 4. (a) Θ-S_A diagram and DIC ($\mu mol \cdot kg^{-1}$). (b) Θ-S_A diagram and $NO_2^- + NO_3^-$ ($\mu mol \cdot kg^{-1}$). (c) Θ-S_A diagram and AOU ($\mu mol \cdot kg^{-1}$). Water masses: Caribbean Surface Water (CSW), Subtropical Underwater (SUW), and Gulf Common Water (GCW). The classification of intermediate and deep-water masses (i.e., TACW, TACWn, AAIW, and NADW) is from Portela et al. (2018).

3.2 Reasons behind the changes in T_θ and σ_θ in the presence or absence of CSW

Seasonal changes in the vertical sections of T_θ and σ_θ occurred above the 26 $kg \cdot m^{-3}$ isopycnal (Fig. A.1). These changes were generally observed with the relatively low temperatures (25.5 ± 1.3 ºC) found at isopycnals above 25.3 $kg \cdot m^{-3}$ in November and March (24.0 ± 1.0 ºC) and in the presence of mixing in the first 150 m of the water column. Additionally, during these months, an average σ_θ of ~ 24.8 ± 0.4 $kg \cdot m^{-3}$ was observed in the upper 170 m of the water column. During the summer, the warmer temperatures (~ 27.0 ± 3.0 ºC) and isopycnal structure (22 and 25.3 $kg \cdot m^{-3}$) showed that CSW was widespread (Fig. A.2).

During the winter of 2013, when small CSW remnants were observed inside the GoM, the ~ 25.3 $kg \cdot m^{-3}$ isopycnal showed high variability within the upper 100 m, while the 24.5 ºC isotherm was barely detected in the region nearest to the LC front (Fig. A.2). In contrast, water with these characteristics was present during the summer when CSW entered the GoM through the LC and was subsequently transported westward via detached LCEs (Fig. A.2).

3.3 AOU and its association with CSW

During the summer, a subsurface DO maximum can be observed in waters with densities less than 25.3 $kg \cdot m^{-3}$ that was not related to the depth of the fluorescence maximum (Fig. 6). This DO maximum was considered to be the boundary between CSW and GCW. However, when thermodynamic effects were removed from observed DO by calculating AOU, the subsurface DO maximum nearly disappeared, indicating that this subsurface maximum was only an effect of T and S caused by enhanced oxygen dissolution during winter (Figs. 6c, 6d, and 6e). During late fall, when the CSW was barely detectable (November 2010), negative AOU concentrations were observed in surface waters (Fig. 6a). In contrast, wind-induced vertical mixing in winter (February/March 2013) resulted in positive AOU values above 25.3 $\mu mol \cdot kg^{-1}$ (Fig. 6b).

Additionally, it was observed that the fluorescence maximum in several profiles (< 0.7 units; denoted by blue contours in Fig. 6) during autumn was detected in the Bay of Campeche and the top 100 m of the water column (Fig. 6a). On the other hand, during winter, the fluorescence maximum was located in a more oceanic region and barely reached 0.3 units (denoted by blue contours) within the first 100 m of the water column (Fig. 6b). With regard to the three summers considered in this study, summer 2015 and summer 2016 showed similar trends, with fluorescence maxima of ~ 0.5 units (denoted by blue contours) located between 50–100 m depth along the majority of the transect (Figs. 6d–e). The summer of 2011 presented its maximum fluorescence near the shelf of the Bay of Campeche, with values < 0.3 units (denoted by blue contours; Fig. 6c). The maximum fluorescence values detected during the three summers do not correspond to the regions where small nuclei with negative AOU values were observed

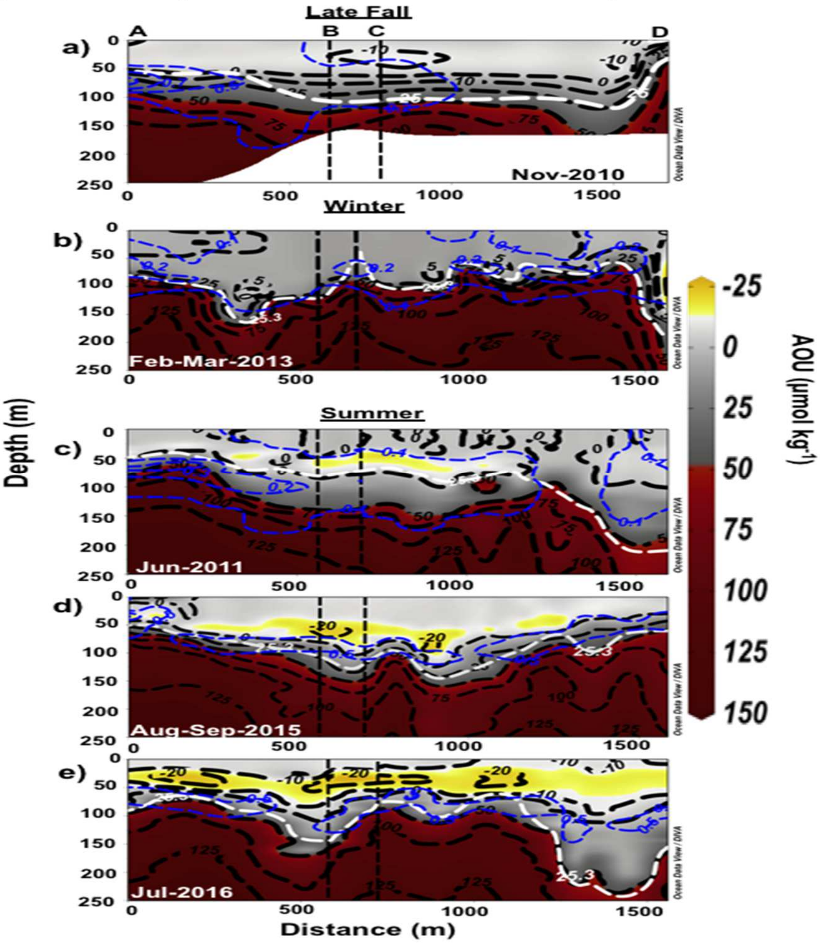

(Figs. 6c–e).

Fig. 6 The vertical distribution (first 250 m of the water column) of apparent oxygen utilization (AOU, µmol·kg^{-1}) is shown for late fall 2010 (a), winter 2103 (b), and summer 2011 (c), 2015 (d), and 2016 (e). The white contours indicate the lower depth limits of Caribbean Surface Water (CSW; 25.3 kg·m^{-3}) in all sections. The location of the transect (letters A and D) is shown in Figure 1c. The blue contours indicate the maximum fluorescence detected at each transect.

3.4 Identification of water masses using the new isopycnal field and thermohaline limits used for the reclassification

The thermohaline ranges associated with SUW were not modified because this water mass was only detected inside the LC (Fig.1a, c, and Fig. A3). Nevertheless, the new thermohaline and chemical characteristics of each water mass are shown in Figures 5 and 7. It is important to highlight that the AOU, nitrate, and DIC ranges presented in Table 1 are considered nominal values. As these variables are measured in shallow waters, they could be affected by several processes, such as biological activity, gas exchange, and the degree of vertical mixing.

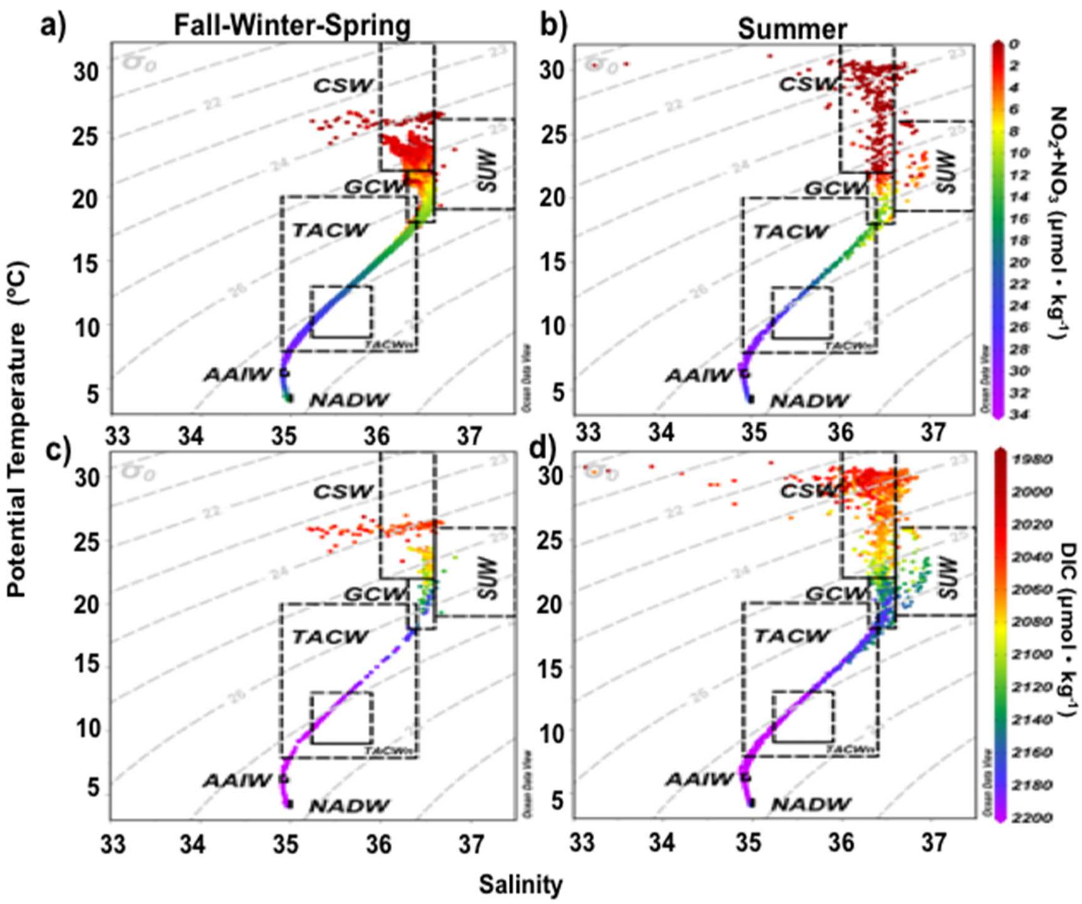

Fig. 7 Potential temperature (T_θ)-salinity (S), nitrate (NO_2^- + NO_3^-, μmol·kg^{-1}; a and b), and DIC (μmol·kg^{-1}, c, and d) diagrams corresponding to the late fall-winter-spring periods of 2010, 2013, and 2016 and summer 2016 and 2017, respectively. The T_θ-S diagrams include data from the GOMECC-3, XIXIMI, Perdido, and Coatzacoalcos regions.

3.4.1. Caribbean Surface Water (CSW)

CSW was detected during the summers of 2011, 2015, 2016, and 2017, in contrast to what was observed during winter. Above the 25.3 kg·m^{-3} isopycnal, AOU concentrations varied between -40 and 50 μmol·kg^{-1}. The T_θ and S range proposed for this water mass are temperatures > 22° C, S values between 36 and 36.6 g·kg^{-1}, nitrate concentrations < 1 μmol·kg^{-1}, and DIC concentrations between 1970–2140 μmol·kg^{-1} (Table 1; Figs. 5, 7, A3).

Table 1. General characteristics of the new classification of surface water masses based on thermohaline and biogeochemical variables [potential temperature (°C), salinity (S; psu and g·kg^{-1}), dissolved oxygen (DO; μmol·kg^{-1}), and apparent oxygen utilization (AOU; μmol·kg^{-1})]. The variability ranges for dissolved inorganic carbon (DIC; μmol·kg^{-1}), nitrate ([NO_2^- + NO_3^-,]; μmol·kg^{-1}), and depth as a function of each water mass identified in the deep region of the GoM are included. The ranges of the temperature and S variables are presented with both oceanographic conventions (EOS-80 and TEOS-10): potential (θ) and conservative (Θ) temperature and psu and absolute salinity (S_A; g·kg^{-1}), respectively.

Water masses	ID	Temperature θ	Θ	S psu	g·kg^{-1}	Sigma (kg·m^{-3})	Mean depth range (m)	DO (µmol·kg^{-1})	AOU (µmol·kg^{-1})	Nitrate (µmol·kg^{-1})	DIC (µmol·kg^{-1})
Caribbean Surface Water	CSW	>22	>22	36–36.6	36.2–36.8	< 25.3	< 170	160–234	-40 to 50	< 1.5	1970–2140
Subtropical Underwater	SUW	19-26	19-26	36.6–37	36.8–37.2	24.5–26.5	100-350	130–220	-5 to 90	1–8	2050–2156
Gulf Common Water	GCW	18–22	18–22	36.3- 36.6	36.5–36.8	25.3–26.3	Winter 0-200 Summer 30-200	110-215	0 to 12	1–14.8	2080-2187
Tropical Atlantic Central Water	TACW	7.9-20	7.9-20	34.9-36-4	35.1-36.6	26.2-27.2	Winter 70-660 Summer 100-780	100-160	73 to 175	8.5–32	2140-2220

3.4.2 Subtropical Underwater (SUW)

We found that SUW was typically present in summer between the 24.5–26.5 kg·m^{-3} isopycnals at depths between 100–350 m, transporting low-oxygen water in regions under the influence of the LC incursion (Fig. 1, A3; Table 1). Figure 5 shows typical oceanographic characteristics of water from the Caribbean, including the salinity maximum present in the Θ-S_A diagrams that describes SUW. The principal thermohaline characteristic of SUW was the presence of an S maximum (~ 36.9) located between 150–250 m that was paired with positive AOU values of ~ 90 µmol·kg^{-1} (Fig. 5c).

3.4.3 Gulf Common Water (GCW)

The new limits for GCW fall between the σ_θ values of 25.3–26.3 kg·m^{-3}, with temperatures between 18–22 ºC, S values between 36.3–36.6 g·kg^{-1}, AOU values between 0–120 µmol·kg^{-1}, nitrate values from 1 to ~15 µmol·kg^{-1}, and DIC concentrations between 2080–2187 µmol·kg^{-1} (Fig. 7 and A3; Table 1). In the GoM, the mixed layer followed a marked seasonal cycle, deepening in winter and shallowing in summer. As such, the Brunt-Väisälä frequency was plotted to evaluate the stability of the water column (Figs. 8b and 8e). Negative Brunt-Väisälä frequency values correspond to portions of the water column with high stability, which was more apparent in winter than in summer. Thus, a lower presence of CSW can be observed during winter (shaded in gray in the T-S diagrams from Figs. 8a and 8d) with GCW near the surface. However, the opposite occurs during summer, with a more notable presence of CSW and deeper GCW.

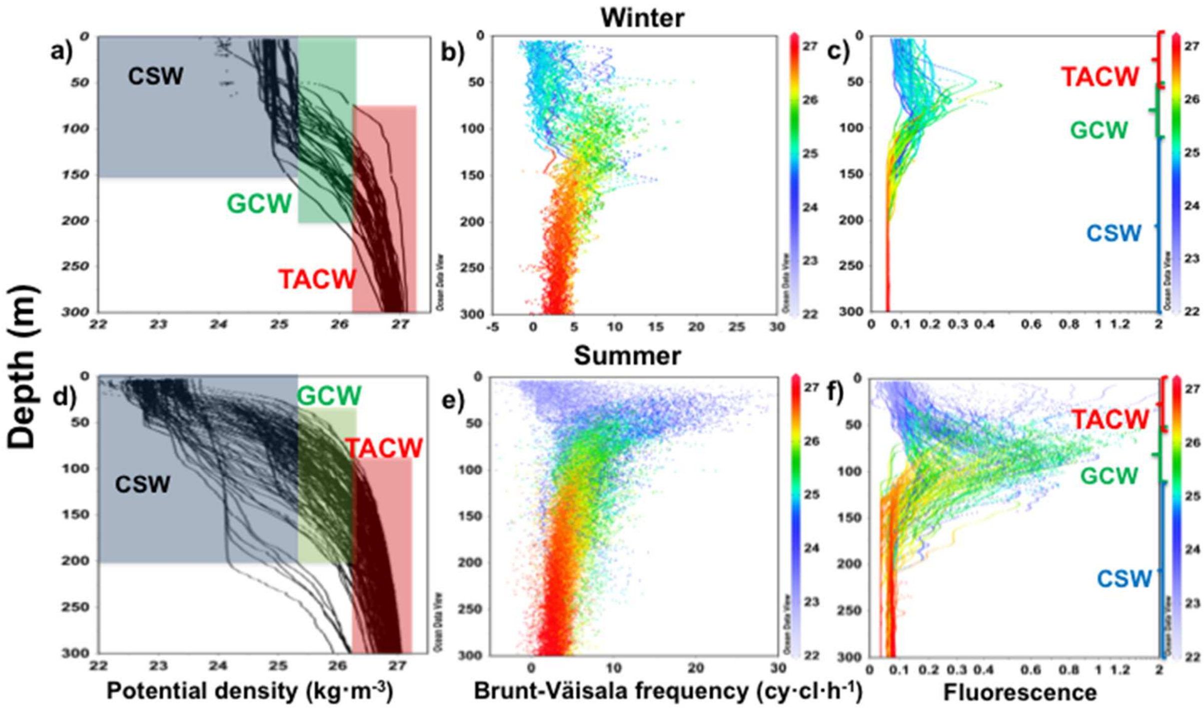

Fig. 8 A comparison of the vertical distributions of potential density (σ_θ, kg·m^{-3}) corresponding to the stations for (a) late fall-winter (2010 and 2013) and (d) summer (2011, 2015, 2016, and 2017). (b and e) The Brunt-Väisälä frequency (cy·cl·h^{-1}) of the water column was estimated for both seasons of the same years. (c and f) A comparison of vertical fluorescence for the same seasons. The blue, green, and red shaded regions indicate the depths of CSW, GCW, and TACW for both seasons.

3.5 Variability in water mass DIC and nitrate concentrations

In general, the near-surface nitrate concentration in SUW was 0.09 µmol·kg^{-1} at a σ_θ value of ~ 25.3 kg·m^{-3}, which increased to 8.0 µmol·kg^{-1} near its defined T_θ-S lower limit. The DIC concentrations were on average 2125 ± 25 µmol·kg^{-1}. The highest nitrate and DIC concentrations within the thermohaline limits of SUW were ~ 8.0 µmol·kg^{-1} and 2156 µmol·kg^{-1}, respectively, which were detected around the σ_θ value of ~ 26.5 kg·m^{-3} and coincided with AOU concentrations of ~ 90 µmol·kg^{-1} (Figs. 5; Table 1).

During summer, CSW was characterized by a low concentration of nitrate (0–1.5 µmol·kg^{-1}) in the first 100 m of the water column (Figs. 7b and 9c; Table 1). Similarly, DIC concentrations fluctuated between 1978–2120 µmol·kg^{-1} (Fig. 7d; Table 1). During winter, CSW presented slightly higher nitrate (0.1–3.8 µmol·kg^{-1}) and DIC (2017–2118 µmol·kg^{-1}) ranges than those detected during summer (Figs. 7a and 7d; Table 1).

GCW presented relatively higher nitrate concentrations during late fall and winter than those observed during summer, with approximately 2.7 µmol·kg^{-1} near 75 m depth (~ 25.4 kg·m^{-3}). The highest nitrate concentration above 180 m (~ 10 µmol·kg^{-1}) was detected during late fall and winter and was observed at the lower limit of GCW and the upper limit of TACW (Fig. 7a,

Table 1). Within GCW, the vertical distribution of DIC mimicked that of nitrate. During late fall and winter, DIC concentrations higher than 2080 μmol·kg^{-1} were found below 50 m, and these reached maximum values of 2187 μmol·kg^{-1} (~ 150 m) close to the lower limit of this water mass (Fig. 7b; Table 1). During summer at 50 m (σ_θ = 25 kg·m^{-3}), DIC values slightly lower than 2095 μmol·kg^{-1} were observed to increase with depth (~ 2176 μmol·kg^{-1} at ~ 100 m; Fig. 7d). The deepening of the nutricline and carbocline observed during summer was associated with the transport of oligotrophic CSW into the GoM with low nitrate values (< 1 μmol·kg^{-1}) near the surface (Figs. 7b and 7d; Table 1).

4 Discussion

A lack of understanding has persisted regarding the formation of GCW and the spatial distribution of SUW within the GoM. This work aimed to understand upper water mass dynamics in the GoM by coupling physical and biogeochemical features. We suggest a reclassification of surface water mass limits above the 26 kg·m^{-3} isopycnal, particularly when the observed thermohaline characteristics overlap, by including biochemical data to obtain a more precise definition of the boundaries of CSW, SUW, and GCW. While the detailed analysis of water masses recently performed by Portela et al. (2018) improved upon the previous classifications, a characterization of the hydrographic and chemical composition of waters above the 26 kg·m^{-3} isopycnal remained deficient. Above this isopycnal, the concentrations of biogeochemical variables, such as AOU, nitrate, and DIC, exhibit significant variation, reflecting water mass origins, mixing, and surface processes.

4.4 Redefinition of the limits between CSW and GCW using T, S, AOU, and nitrate

Our results indicate that the intrusion of CSW was associated with the maximum phase of LC extension and LCE transport and a decrease in the supply of CSW during late fall and winter. Previous studies have consistently shown an asymmetrical biannual variation in the growth and wane of the LC (i.e., strong from summer to fall and weak from winter to spring), with the asymmetry reflecting long-term wind data (Chang and Oey, 2013). Zeng et al. (2015) have shown the existence of three patterns throughout the year that consist of normal LC conditions without extension or shedding (January–May), a transitional period (July–August), and a period of retraction (September–December). Additionally, based on ADT and chlorophyll data, Delgado et al. (2019) reported that CSW is primarily transported into the GoM during the maximum phase of the extension of the LC in summer, while CSW transport is minimal in winter. Here, we emphasize the critical roles of the LC, the Yucatan Current, and the spread of the LCEs into the GoM when explaining the increase (decrease) of CSW in the GoM.

Portela et al. (2018) defined the T-S limits of CSW within the GoM, renaming it CSWr and delimiting its range between 50–150 m, after excluding surface waters above 50 m depth. However, the overlap in the thermohaline ranges of CSW and GCW was overlooked (Fig. 2) by Portela et al. (2018), and a seasonal analysis of the distribution of water masses was excluded. This is needed to determine when or if these water masses are present. Here, we propose that the top 50 m of the water column should be included in the classification of CSW (Table 1). Also, when the overlap between water mass limits is observed, it must be assumed that mixing is present and that values closer to the core of the water mass (considering sub-surface values) will better define its limits. This may have important implications when using water mass mixing models, as overlapping limits reduce the ability to discriminate between water masses and suggest the presence of diffusive mixing processes, which may lead to a misinterpretation of the mechanisms used to explain biogeochemical processes. Our results show that CSW and GCW can be differentiated by considering nitrate and AOU concentrations at the upper and lower limits of GCW and CSW, respectively. However, this approach assumes that AOU and nitrate behave conservatively (i.e., their concentration and vertical distribution in the gulf are mainly controlled by physical processes). Thus, we suggest the following mechanism to explain the apparent conservative behavior of AOU and nitrate.

During fall and winter, the LC rarely extends into the GoM. At the same time, intense seasonal northerly winds (i.e., Nortes) occur and mix GCW subsurface waters with CSW, spreading inside the gulf through LCEs. As a result, the estimated AOU in GCW during the winter months showed either a trend towards positive values or an equilibrium with the atmosphere due to strong vertical mixing, with subsurface waters with high microbial respiration, remineralization, and nitrate concentrations being transported to the surface (Figs. 6a–b, Fig. 9f, and 10a–b). In contrast, during spring–summer, the most significant extension of the LC results in the advection of warm and oligotrophic CSW (nitrate < 1 μmol·kg^{-1}) with negative AOU values to the interior of the GoM by westward-moving LCEs (Biggs and Ressler, 2001; Delgado et al., 2019) above GCW (Figs. 4, 5, 6c–d, and 9c–f).

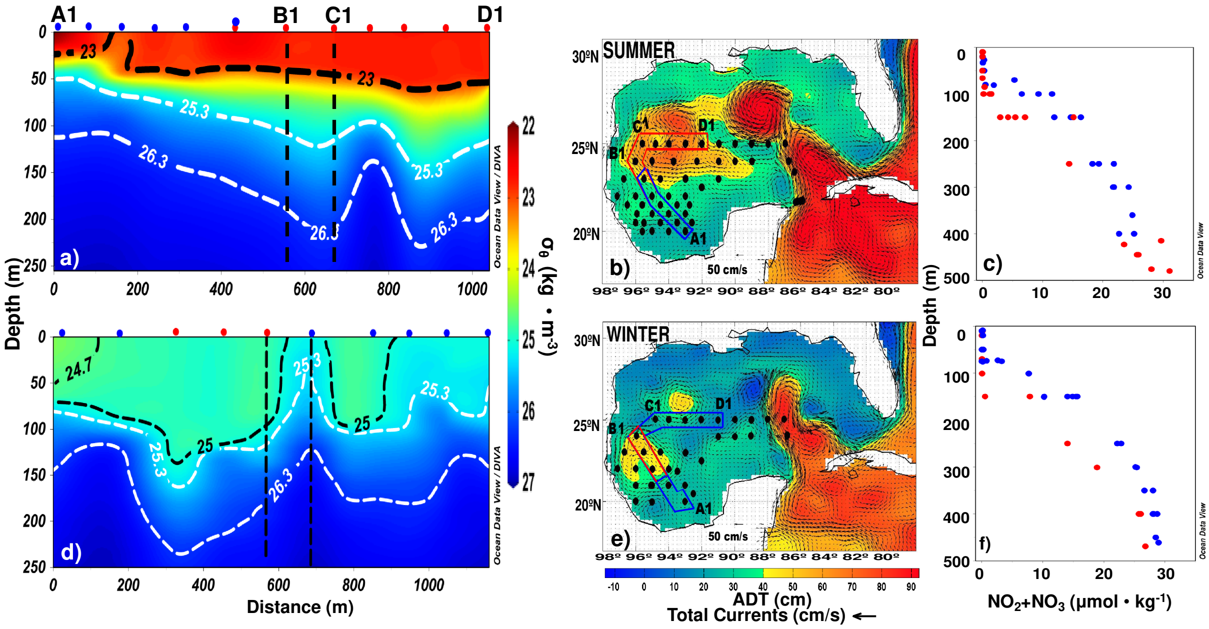

Fig. 9 Vertical distribution (250 m) of potential density (kg·m^{-3}) for summer 2015 (a) and winter 2013 (d). White contours indicate the lower limits of CSW [25.3 kg·m^{-3}; (a)] and GCW [26.3 kg·m^{-3}; (d)] in both sections. The ADT maps show the trajectory of the summer (b) and winter (e) sections of each cruise. The nitrate profiles (μmol·kg^{-1}; c = summer; f = winter) only include the stations found within the trajectory traced in the ADT maps for each cruise. The blue and red dots indicate the stations found outside the areas influenced by anticyclonic eddies and those in the area influenced by anticyclonic gyres, respectively.

CSW is always less dense than GCW, mainly due to the higher temperatures acquired in the Caribbean basin. Moreover, CSW has lower DO concentrations than those found in the surface waters of the GoM in winter, which is also due to temperature-related differences in solubility that lead to negative AOU values (up to ~ -40 $\mu mol \cdot kg^{-1}$; Benson and Krause, 1984). The warm temperature of CSW induces stratification that limits the exchange of oxygen with underlying GCW (Figs. 6c–d and 8d). Therefore, AOU (< 50 $\mu mol \cdot kg^{-1}$; Table 1) and nitrate concentrations (< 1 $\mu mol \cdot kg^{-1}$) can be used to indicate the boundary between CSW and GCW (Fig. 5; Table 1).

4. 1. 1. On the formation of GCW

The presence of GCW near or at the surface during autumn and winter was caused by 1) a weakening of the CSW signal towards the interior of the GoM due to the retraction of the LC and the dissipation of the LCEs, and 2) the strong winds that result in a well-defined and deep (100 m) mixed layer. This last observation has been previously noted by Nowlin and McLellan (1967), Elliott (1979, 1982), Vidal et al. (1994), and Portela et al. (2018). It has been suggested that GCW formation takes place on the western slope of the GoM (where the LCEs dissipate) as well as during winter when the wind regime produces a mixed layer of approximately 100 m that dilutes SUW (Vidal et al., 1992, 1994; Portela et al., 2018). New information regarding GCW formation was reported by Sosa-Gutierrez et al. (2020), who indicated that GCW formation was due to the progressive erosion of the high-salinity cores of LCEs during their westward journeys across the gulf. However, our results suggest GCW formation originates from the mixing of CSW with TACW in the western side of the GoM and not with SUW, as was reported by Vidal et al. (1994). Our conclusion was based on the distribution of SUW-T-S data from all cruises, which shows that SUW occurrence is restricted to the region influenced by the LC (Figs. 1 and 10).

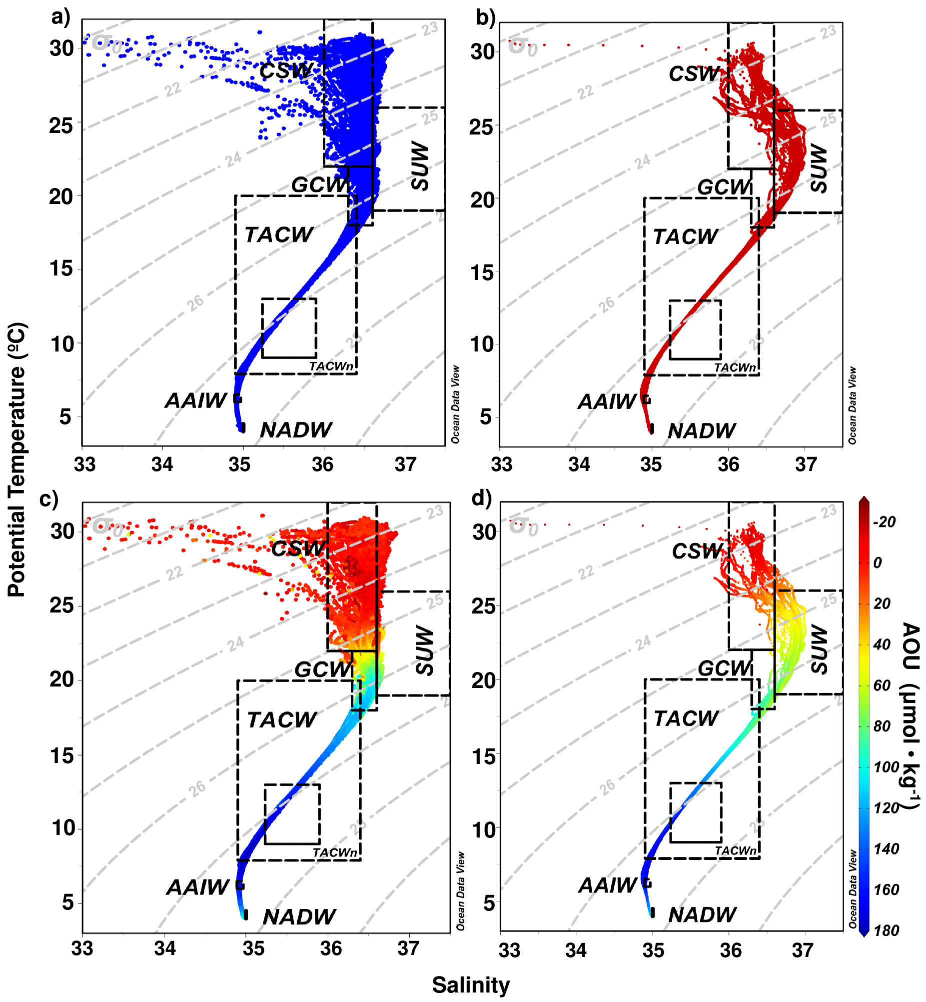

Fig. 10 Potential temperature (T_θ)-salinity (S) diagrams of data from the six XIXIMI (2010–2017) cruises, GOMECC-3 (2017) cruise, and two Perdido and Coatzacoalcos (2016) cruises. (a) T_θ-S diagram with blue dots denoting characteristics of the western region of the gulf. (b) T_θ -S diagram with red dots denoting the influence of LC incursion and the characteristic SUW signal. (c) T_θ-S diagram and apparent oxygen utilization (AOU, μmol·kg^{-1}) diagram with characteristics of the gulf (blue dots). (d) T_θ-S diagram and AOU (μmol·kg^{-1}) diagram with characteristics of the SUW signal (red dots). The distribution of the upper water masses was based on the new adjustments proposed in this study (water masses: CSW, GCW, and SUW). For deep waters, the classification proposed by Portela et al. (2018) using T_θ and S was used (water masses: TACW, TACWn (core), AAIW, and NADW).

During winter, when CSW was almost undetectable in some of the internal and western regions of the GoM, it was found that TACW (> 70 m; Table 1; Fig. A.1c) may become shallower compared to its depth during summer (> 100 m; Figs. 8a, 8d, 9c, 9f, and Fig. A.1). Thus, the proximity of TACW and GCW will promote an alternating pattern that will eventually affect biological productivity due to the availability of nutrients in the water column (Figs. 7b, 7d, and 9c; Muller-Karger et al., 2015; Pasqueron et al., 2018; Damien et al., 2018). At the same time, convective mixing leads to low DO concentrations, and thus the positive AOU concentrations that are characteristic of TACW are reflected in GCW. In addition, noticeable increases in nitrate and DIC concentrations and a fluorescence maximum near the surface were observed (Figs. 7 and 8c). In contrast, during summer and in the presence of CSW, the mixed layer lay above the nutricline, and the fluorescence maximum was associated with the depth of GCW (Fig. 8f).

As the LC enters the GoM and LCEs are shed and migrate into the gulf during the summer months, oligotrophic waters dominate the first 100 m of the water column. Some studies have shown that low chlorophyll concentrations accompany the incursion of warm water into the gulf (Muller-Karger et al., 2015; Linacre et al., 2015). In contrast, periods of low temperatures and strong winds coincide with high chlorophyll concentrations and primary productivity (Muller-Karger et al., 2015). Furthermore, satellite observations have detected maximum chlorophyll concentrations in winter (Pasqueron et al., 2017). This agrees with the results of Damien et al. (2018), who explained that the winter increase in the integrated chlorophyll concentration was due to nutrient injections to the euphotic layer, reflecting a deepening of the mixed layer.

4. 1. 2. Surface water masses modulate the depth of the nutricline

One biological implication of the presence of CSW is that it is oligotrophic. In summer, it can be found at depths up to 100 m, which can be seen in Figure 9, wherein we compare the vertical distribution of nitrate and potential density with ADT maps for summer 2015 (when mesoscale eddies were abundant) and winter 2013 (when the number and spatial extent of eddies were low). During summer, a near-surface incursion of low-potential density water associated with CSW was observed (isopycnal of 25.3 $kg \cdot m^{-3}$, white color; Fig. 9a). This incursion brought water with oligotrophic characteristics to depths shallower than 70 m (nitrate between 0–0.5 $\mu mol \cdot kg^{-1}$; Fig. 9c). Also, the vertical distribution of the nitrate concentration was reduced by the entrance of the LC and the subsequent shedding of LCEs carrying CSW into the interior of the gulf (Figs. 9). With the winter retraction of the LC and accompanying dissipation of LCEs, the CSW signal decreased, breaking the stratification pattern observed in summer (Figs. 8a–b). This favors a deeper mixed layer with high potential density values in the first 200 m of the water column, in which GCW predominates and nutrients are pumped to surface waters (Fig. 9d).

The results of the analysis carried out using the CARS2009 database to evaluate the temporal changes in CSW and GCW are shown in Figure A.3, and the climatological averages in winter (February) and summer (July) are contrasted. The T_θ-S diagram, in addition to the vertical sections showing the position of the 25.3 $kg \cdot m^{-3}$ isopycnal, indicates a higher volume of CSW occupying the surface layer during summer. During winter, the results show that the volume and presence of CSW were reduced, giving way to a greater dominance of GCW, which was detected in some gulf regions from the surface to ~ 200 m depth. This independently supports our observation that the extension (retraction) of the LC favors the deepening (shallowing) of the nutricline during summer (winter). Also, the analysis of CARS2009 climatological data confirms the importance of CSW for determining the near-surface biogeochemical characteristics of the GoM. All cruise data, including the CARS2009 climatological data, support that nitrate and AOU can be used to define the lower limit of CSW.

4.1.3 Benefits of the new reclassification

One contribution of the new reclassification is a better understanding of how GCW is formed. Recently, it has been suggested that as of 2003, larger volumes of CSW have invaded the western portion of the GoM (Delgado et al., 2019), and the addition of biogeochemistry to define the various water masses particularly when the observed thermohaline characteristics overlap. Finally, the new proposed potential density and thermohaline limits of near-surface water masses in the GoM may promote future research efforts focused on the relevance of biogeochemical processes at small scales.

5 Conclusion

In the western region of the GoM, the GCW is not solely formed by the mixing of CSW and SUW but mainly by the mixing of remnant CSW with TACW. In winter, the CSW mixed with GCW, and the biogeochemical composition of surface waters was affected. The presence of GCW near and at the surface during autumn and winter was caused by a weakening of the CSW signal towards the interior of the GoM due to the retraction of the LC and the dissipation of LCEs and because of strong winds that result in a well-defined and deep mixed layer.

GCW and SUW were also redefined and characterized based on differences in AOU, nitrate, and DIC concentrations. The new limits proposed for CSW, SUW, and GCW have been instrumental in clarifying the dynamics of the surface waters of the GoM while allowing for clear separations. This new reclassification of the limits of the waters above the 26 $kg\cdot m^{-3}$ isopycnal has resulted in a modification of the present thermohaline ranges defining CSW, SUW, and GCW.

One of the biogeochemical implications of the presence or absence of CSW was that this modulates the depth of the nutricline and likely influences primary productivity. This water mass was detected mainly during the summer months, with a lower limit marked by negative AOU concentrations.

Acknowledgments

We thank two anonymous reviewers for their positive criticisms and comments that helped us improve the manuscript significantly.The study was funded by the Mexican National Council for Science and Technology - Mexican Ministry of Energy - Hydrocarbon Fund [project 201441]. This is a contribution of the Gulf of Mexico Research Consortium (CIGoM). We acknowledge PEMEX's specific request to the Hydrocarbon Fund to address the environmental effects of oil spills in the Gulf of Mexico. In addition, LB received support from the NOAA Ocean Acidification Program. This research was carried out in part under the auspices of the Cooperative Institute for Marine and Atmospheric Studies under cooperative agreement #NA10OAR4320143. We thank the crew of the B/O *Justo Sierra* for their professional support and experience. We would also like to thank Dr. Juan Carlos Herguera for his role in oxygen CTD data calibration and Dr. Esther Portela for her constructive criticism and suggestions. The Data Unification and Altimeter Combination System have produced Altimeter products available on the AVISO (Archiving, Validation, and Interpretation of Satellite Oceanographic data) website (https://www.aviso.altimetry.fr/en/data). Wind stress, geostrophic data, and Ekman currents were extracted from GEKCO (Geostrophic Ekman Current Observatory; Sudre et al., 2013; http://www.legos.obs-mip.fr/members/sudre/gekco_form) with support from LEGOS. Three sources were used for the wind stress GEKCO product: 1) 01/01/1993–27/10/1999 period (https://www.ncdc.noaa.gov/data-access/marineocean-data/blended-global/blended-sea-winds), 2) 28/10/1998–20/03/2007 period (MWF L3 daily QuikSCAT product; http://cersat.ifremer.fr0),

and 3) 21/03/2007–31/12/2017 period (MWF L3 daily ASCAT product; http://cersat.ifremer.fr/data/products/catalogue). Finally, the general features of the Gulf of Mexico Loop Current eddies were taken from https://www.horizonmarine.com/loop-current-eddies.

References

Baird R. & Bridgewater L., 2017. *Standard methods for the examination of water and wastewater.* 23rd edition. Washington, D.C.: American Public Health Association.

Barbero, L., Pierrot, D., Wanninkhof, R. *et al.* (2019) Third Gulf of Mexico ecosystems and carbon cycle (GOMECC-3) cruise. doi: doi.org/10.25923/y6m9-fy08.

Becker, S.; Aoyama, M.; Woodward, E.M.S.; Bakker, K.; Coverly. S.; Mahaffey, C. and Tanhua, T. (2019) GO-SHIP Repeat Hydrography Nutrient Manual: The precise and accurate determination of dissolved inorganic nutrients in seawater, using Continuous Flow Analysis methods. In: The GO-SHIP Repeat Hydrography Manual: A Collection of Expert Reports and Guidelines. Available online at: http://www.go-ship.org/HydroMan.html. DOI: http://dx.doi.org/10.25607/OBP-555

Benson, B.B. & Krause, D., 1984. The concentration and isotopic fractionation of oxygen dissolved in freshwater and seawater in equilibrium with the atmosphere. *Limnology and Oceanography*, 29(3), 620–632. https://doi.org/10.4319/lo.1984.29.3.0620

Biggs, D. C. & Ressler, P. H., 2001. Distribution and abundance of phytoplankton, zooplankton, ichthyoplankton, and micronekton in the deepwater Gulf of Mexico. *Gulf of Mexico Science*, 2001(1), 7–29. http://doi.org/10.18785/goms.1901.02

Brokaw, R. J., Subrahmanyam, B., & Morey, S. L., 2019. Loop current and eddy-driven salinity variability in the Gulf of Mexico. *Geophysical Research Letters*, 46(11), 5978-5986. https://doi.org/10.1029/2019GL082931

Broecker, W. S. and T. H. Peng, 1982. Tracers in the Sea, Eldigio Press, Palisades, N.Y., 690 pp.

Bunge, L., Ochoa, J., Badan, A., Candela, J., & Sheinbaum, J., 2002. Deep flows in the Yucatan Channel and their relation to changes in the Loop Current extension. *Journal of Geophysical Research*, 107, C12. https://doi.org/10.1029/2001JC001256

Carrillo, L., Johns, E. M., Smith, R. H., Lamkin, J. T., & Largier, J. L., 2016. Pathways and hydrography in the Mesoamerican Barrier Reef System Part 2: Water masses and thermohaline structure. *Continental Shelf Research*, 120, 41–58. http://doi.org/10.1016/j.csr.2016.03.014

Chang, Yu-Lin & Oey, Lie-Yauw, 2013. Loop Current Growth and Eddy Shedding Using Models and Observations: Numerical Process Experiments and Satellite Altimetry Data. Journal of Physical Oceanography. 43. 669-689. https://doi.org/10.1175/JPO-D-12-0139.1

Delgado, J. A., Sudre, J., Tanahara, S., Montes, I., Hernandez-Ayon, J. M., & Zirino, A., 2019. Effect of Caribbean Water incursion into the Gulf of Mexico derived from absolute dynamic topography, satellite data, and remotely sensed chlorophyll a. *Ocean Science*, 15(6), 1561-1578. https://doi.org/10.5194/os-2019-58

Damien, P., Pasqueron de Fommervault, O., Sheinbaum, J., Jouanno, J., Camacho-Ibar, V. F., & Duteil, O., 2018. Partitioning of the Open Waters of the Gulf of Mexico Based on the Seasonal and Interannual Variability of Chlorophyll Concentration. *Journal of Geophysical Research: Oceans*, 123(4), 2592–2614. http://doi.org/10.1002/2017JC013456

Dickson, A.G., Sabine, C.L., & Christian, J.R. (Eds.), 2007. *Guide to Best Practices for Ocean CO2 Measurements*, PICES Special Publication. Sidney, Canada: North Pacific Marine Science Organization.

Elliott, B. A., 1982. Anticyclonic Rings in the Gulf of Mexico. *Journal of Physical Oceanography*, 12, 1292-1309. https://doi.org/10.1175/1520-0485(1982)012<1292: ARITGO>2.0.CO;2

Gallegos, A., 1996. Descriptive physical oceanography of the Caribbean Sea. Small Islands: Marine Science and Sustainable Development Coastal and Estuarine Studies. *American Geophysical Union*, 51, 36–55.

Garcia, H.E. and R.E. Keeling, 2001. On the global oxygen anomaly and air-sea flux. J. Geophys. Res., 106, 31155-31166

El-Sayed, S. Z., 1972. Primary productivity and standing crop of phytoplankton. In: Bushnell, V. C. (Ed.), *Chemistry, primary productivity, and benthic algae of the Gulf of Mexico* (pp. 8–13 pp.) New York, NY: American Geographical Society.

Hall, C. A. & R. R. Leben., 2016. Observational evidence of seasonality in the timing of Loop Current eddy separation. *Dynamics of Atmospheres and Oceans*, 76, 240–267. https://doi.org/10.1016/j. dynatmoce.2016.06.002

Hamilton, P., Leben, R., Bower, A., Furey, H., & Pérez-Brunius, P., 2018. Hydrography of the Gulf of Mexico using autonomous floats. *Journal of Physical Oceanography*, 48, 773–794. https://doi.org/10.1175/JPO-D-17-0205.1

Heileman, S., & Rabalais, N., 2009. XV-50 Gulf of Mexico LME# 5. In: Sherman, K., Hempel, G. (Eds.) The UNEP Large Marine Ecosystem Report: A perspective on the changing condition in LMEs of the world's Regional Seas. United Nations Environment Program, Nairobi, Kenya, pp. 673–688, UNEP Regional Seas Report and Studies. (182).

Herring, J. H., 2010. Gulf of Mexico hydrographic climatology and method of synthesizing subsurface profiles from the satellite sea surface height anomaly. US Department of Commerce. National Oceanic and Atmospheric Administration. National Ocean Service. Coastal Survey Development Laboratory (Report 122, pp. 1-63)

Huang, W.J., Cai, W.J., Powell, R.T., Lohrenz, S.E., Wang, Y., Jiang, L.Q., Hopkinson, C.S., 2012. The stoichiometry of inorganic carbon and nutrient removal in the Mississippi River plume and adjacent continental shelf. Biogeosciences. 9, 2781–2792. doi: 10.5194/bg-9-2781-2012

Hydes, D. J., Aoyama, M., Aminot, A., Bakker, K., Becker, S., Coverly, S. et al., 2010. Determination of dissolved nutrients (N, P, Si) in seawater with high precision and inter-comparability using das-segmented continuous flow analyzers. In: Hood EM, Sabine CL, Sloyan BM (Eds.) *The GO-SHIP repeat hydrography manual: a collection of expert* *reports and guidelines* (IOCCP Report 14, ICPO publication series number 134) Paris, France: UNESCO-IOC. http://www.go-ship.org/HydroMan.html

Intergovernmental Oceanographic Commission, 2010. The international thermodynamic equation of seawater 2010: Calculation and use of thermodynamic properties. Intergovernmental Oceanographic Commission Manuals and Guides 56, UNESCO, 196 pp.

Ito, T., M. Follows, and E. A. Boyle, 2004. Is AOU a good measure of respiration in the oceans? Geophys. Res. Lett., 31, doi:10.1029/2004GL020900

Jochens, A. E., & DiMarco, S. F., 2008. Physical oceanographic conditions in the deepwater Gulf of Mexico in summer 2000–2002. *Deep-Sea Research Part II: Topical Studies in Oceanography*, 55(24–26), 2541–2554. https://doi.org/10.1016/j.dsr2.2008.07.003

Johnson, K. M., Williams, P. J., Brändström, L. & Sieburth, J. M., 1987. Coulometric TCO2 analysis for marine studies: Automation and calibration. *Marine Chemistry*, 21, 117–133, https://doi.org/10.1016/0304-4203(87)90033-8

Lorena Linacre, R. Lara-Lara, V. Camacho-Ibar, J. C. Herguera, C. Bazán-Guzmán, V. Ferreira-Bartrina (2015). Distribution pattern of picoplankton carbon biomass linked to mesoscale dynamics in the southern Gulf of Mexico during winter conditions. *Deep-Sea Research Part I: Oceanographic Research,*106 (55-67). https://doi.org/10.1016/j.dsr.2015.09.009

Martínez-López B. and J. Zavala-Hidalgo., 2009. Seasonal and interannual variability of cross-shelf transports of chlorophyll in the Gulf of Mexico. *Journal of Marine Systems*, 77, 1-20. DOI: 10.1016/j.jmarsys.2008.10.002

McDougall, T. J., & Barker, P. M., 2011. *Getting started with TEOS-10 and the Gibbs Seawater (GSW) Oceanographic Toolbox.* SCOR/IAPSO WG127.

Merrell, W. J., & Morrison, J. M., 1981. On the circulation of the western Gulf of Mexico with observations from April 1978. *Journal of Geophysical Research*, 86(C5), 4181–4185. https://doi.org/10.1029/JC086iC05p04181

Morrison, J. M., Merrel, W. J., Key, R. M., & Key, T. C., 1983. Property distributions and deep chemical measurements within the western Gulf of Mexico. *Journal of Geophysical Research*, 88(C4), 2601–2608. https://doi.org/10.1029/JC088iC04p02601

Morey, S. L., Martin, P. J., O'Brien, J. J., Walclraft, A. A., & Zavala-Hidalgo, J., 2003a. Export pathways for river discharged fresh water in the northern Gulf of Mexico. *Journal of Geophysical Research*, 108(C10), 3303. https://doi.org/10.1029/2002JC001674

Morey, S. L., Schroeder, W. W., O'Brien, J. J., & Zavala-Hidalgo, J., 2003b. The annual cycle of riverine influence in the eastern Gulf of Mexico basin. *Geophysical Research Letters*, 30(16), 1–4. http://doi.org/10.1029/2003GL017348

Muller-Karger, F.E., Smith, J.P., Werner, S., Chen, R., Roffer, M., Liu, Y., Muhling, B., Lindo-Atichati, D., Lamkin, J., Cerdeira-Estrada, S., Enfield, D.B., 2015. Natural Variability of Surface Oceanographic Conditions in the Offshore Gulf of Mexico. Prog. Oceanogr. http://dx.doi.org/10.1016/j.pocean.2014.12.007

Nowlin, W. D. Jr., 1972. Winter circulation patterns and property distributions. In: Capurro, L. R. A. & Reid, J. L. (Eds.) *Contributions on the Physical Oceanography of the Gulf of Mexico* (3-51). College Station, TX: Texas A & M University Oceanographic Studies.

Oey, L.-Y., T. Ezer, and H.-C. Lee., 2005. "Loop Current, Rings and Related Circulation in the Gulf of Mexico: A Review of Numerical Models and Future Challenges." In Circulation in the Gulf of Mexico: Observations and Models, edited by W. Sturges, and A. Lugo-Fernandez, 31–56. Washington, DC: American Geophysical Union.

Pasqueron De Fommervault, O., Pérez-Brunius, P., Damien, P., Camacho-Ibar, V. F., & Sheinbaum, J., 2017. Temporal variability of chlorophyll distribution in the Gulf of Mexico: Bio-optical data from profiling floats. *Biogeosciences*, 14(24), 5647–5662. http://doi.org/10.5194/bg-14-5647-2017

Pérez-Brunius, P., García-Carrillo, P., Dubranna, J., Sheinbaum, J., & Candela, J., 2013. Direct observations of the upper layer circulation in the southern Gulf of Mexico. *Deep Sea Research Part II: Topical Studies in Oceanography*, 85, 182-194. https://doi.org/10.1016/j.dsr2.2012.07.020

Pytkowicx, Ricardo M., 1971. On the Apparent Oxygen Utilization and the Preformed Phosphate in the Oceans, Limnology and Oceanography, 16, doi: 10.4319/lo.1971.16.1.0039.

Portela, E., Tenreiro, M., Pallàs-Sanz, E., Meunier, T., Ruiz-Angulo, A., Sosa-Gutiérrez, R., & Cusí, S., 2018. Hydrography of the central and western Gulf of Mexico. *Journal of Geophysical Research: Oceans*, 1–16. http://doi.org/10.1029/2018JC013813

Schmitz, W. J. J., 2005. Cyclones and westward propagation in the shedding of anticyclonic rings from the Loop Current. *Circulation in the Gulf of Mexico: Observations and Models, Geophys. Monogr.,* Vol. 161, Amer. Geophys. Union, 241–261.

Schmitz, W. J. J. and Richardson P.L., 1991. On the sources of the Florida Current. Deep-Sea Research Part A. Oceanographic Research Papers, 38, 379-409. https://doi.org/10.1016/S0198-0149(12)80018-5.

Sosa-Gutiérrez, R., Pallàs-Sanz, E., Jouanno, J., Chaigneau, A., Candela, J., & Tenreiro, M. (2020). Erosion of the subsurface salinity maximum of the Loop Current Eddies from glider observations and a numerical model. Journal of Geophysical Research: Oceans, 125, e2019JC015397. https:// doi.org/10.1029/2019JC015397.

Sturges, W. & Leben, R., 2000. Frequency of ring separations from the Loop Current in the Gulf of Mexico: A revised estimate, *Journal of Physical Oceanography*, 30, 1814–1819. DOI: 10.1175/1520-0485(2000)030<1814: FORSFT>2.0.CO2

Vidal, V. M. V, Vidal, F. V, & Pérez-Molero, J. M., 1992. Collision of a loop current anticyclonic ring against the continental shelf-slope of the western Gulf of Mexico. *Journal of Geophysical Research: Oceans*, 97(C2), 2155–2172. http://doi.org/10.1029/91JC00486

Vidal, V. M. V., Vidal, F. V., Hernández, A. F., Meza, E., & Zambrano, L., 1994. Winter water mass distributions in the western Gulf of Mexico affected by a colliding anticyclonic ring. *Journal of Oceanography*, 50(5), 559–588. http://doi.org/10.1007/BF02235424

Xiangming Zeng, Yizhen Li, Ruoying He & Yuqi Yin., 2015. Clustering of Loop Current patterns based on the satellite-observed sea surface height and self-organizing map. Remote Sensing Letters, 6:1, 11-19, DOI: 10.1080/2150704X.2014.99834

Appendices

Fig. A.1. A comparison of fall (a), winter (c), and summer (b, d, and e) regarding the variability of the depth of 26 kg·m^{-3} density field in the GoM (in situ hydrographic data collected in November 2010, July 2011, February/March 2013, August/September 2015, and June 2016).

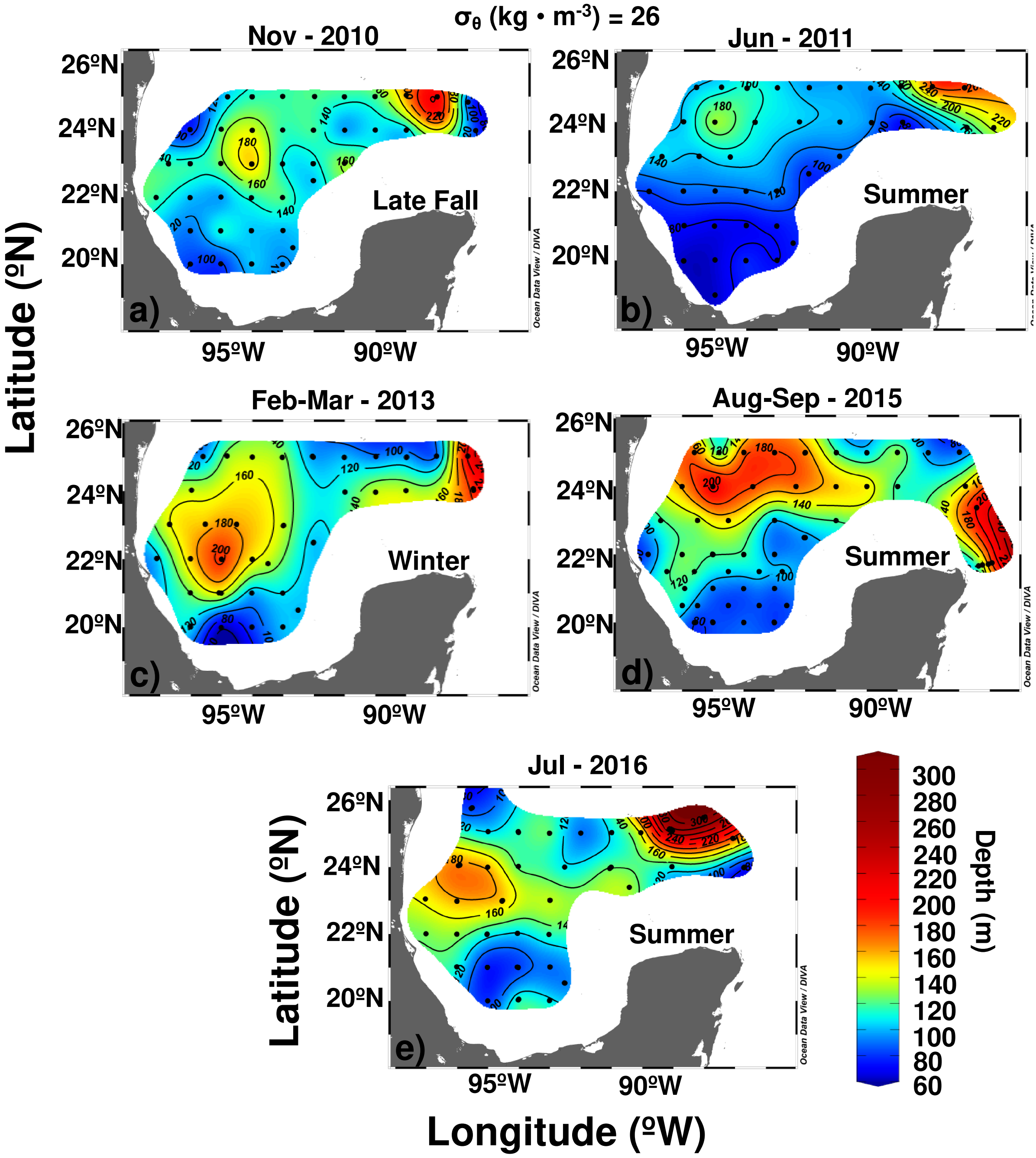

Fig. A.2. The vertical distribution (first 250 m) of potential temperature (ºC) and potential density ($kg \cdot m^{-3}$) shown for late fall 2010 (a and f), winter 2013 (b and g), and summer 2011 (c and h), 2015 (d and i), and 2016 (e and j). The location of the transect is shown in Figure 1c.

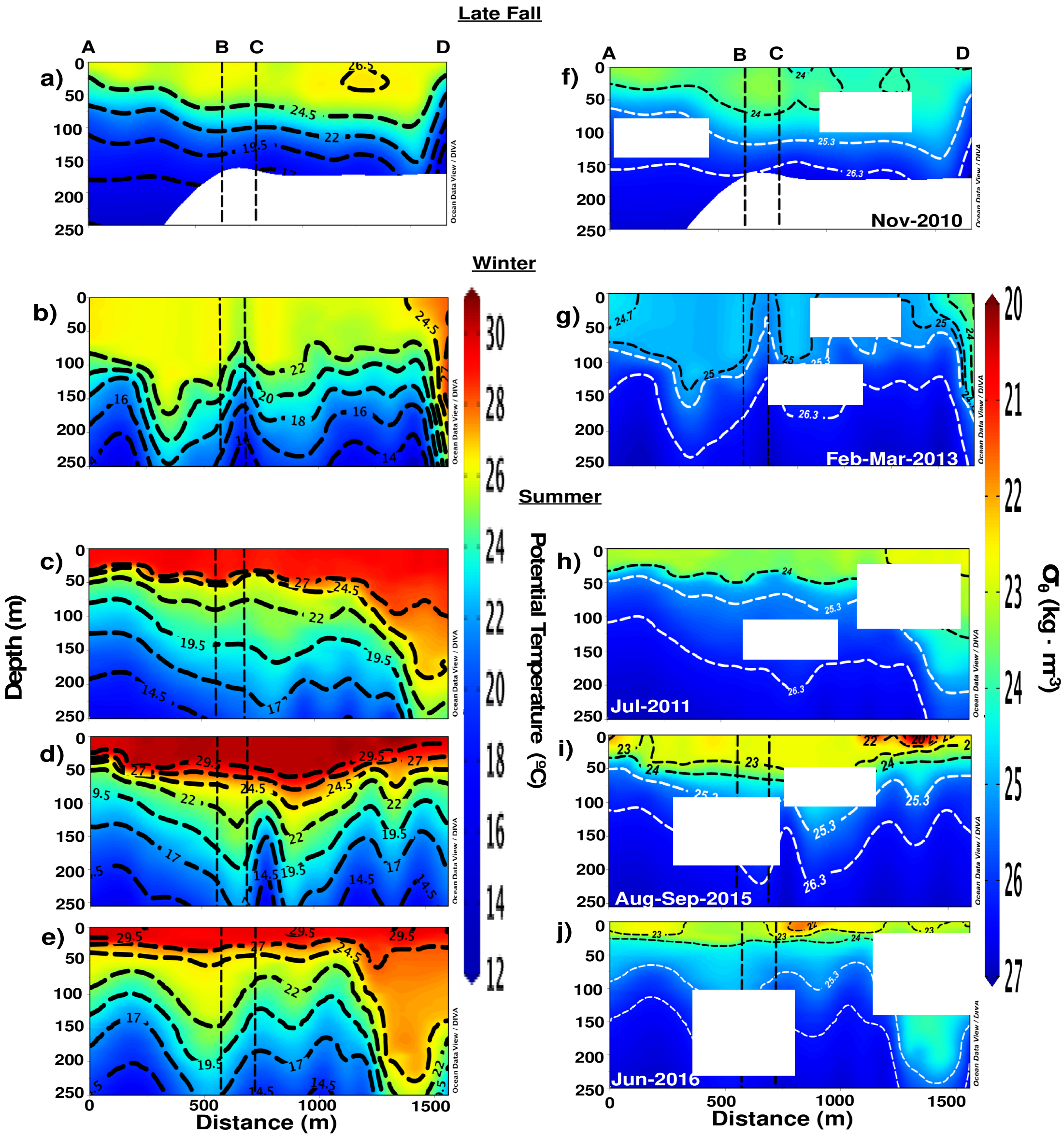

Fig. A.3. Potential temperature (T_θ)-salinity (S) diagram vs. apparent oxygen utilization (AOU) [$\mu mol \cdot kg^{-1}$] annual diagrams for February (a) and July (b) showing the newly adjusted thermohaline range limits proposed in this study. Data derived from the CARS-2009 database. Annual vertical sections (-95.5 to -86.5 ºW, 25 ºN; the section shown in Figure 1c from station C to E) of AOU [$\mu mol \cdot kg^{-1}$] and nitrate [µM] concentrations for February (c, and d) and July (e, and f) derived from the CARS-2009 database. The AOU and nitrate sections include the 10 $\mu mol \cdot kg^{-1}$ isopycnal and 10 µM, respectively. In addition, each section includes the 25 $\mu mol \cdot kg^{-1}$ isopycnal (white line), denoting the lower limit of CSW.